Simulation of Hydrodynamic Wave Loading by a Compressible Two-Phase Flow Method

Rik Wemmenhove
Schlumberger
P.O. Box 234, 1372 Asker
Norway
rwemmenhove@slb.com

Roel Luppes, Arthur E.P. Veldman
Institute for Mathematics and Computer Science
University of Groningen
P.O. Box 407, 9700AK Groningen
The Netherlands
{r.luppes, a.e.p.veldman}@rug.nl

Tim Bunnik
MARIN
P.O. Box 28, 6700 AA Wageningen
The Netherlands
t.bunnik@marin.nl

***Abstract*—Hydrodynamic wave loading on offshore structures is studied by carrying out numerical simulations. Particular attention is paid to complex hydrodynamic phenomena such as wave breaking and air entrapment. The applied CFD code, COMFLOW, solves the Navier–Stokes equations and uses an improved Volume-Of-Fluid method to track the movement of the free surface. Application of two different fluid models, single-phase (only liquid) and two-phase (liquid and a compressible gas) is presented, the latter model being capable of simulating bubbles of gas entrapped in liquid.**

The free surface tracking uses a local height function to keep the surface sharp. A newly-developed gravity-consistent density averaging method is applied to prevent spurious velocities around the free surface. Time integration is carried out with a generalization of the familiar pressure-correction method, in which the full acoustical part of the flow equations (continuity equation and pressure gradient) is treated implicitly.

Numerical results are verified against experimental data for two test cases. As an example of internal wave loading, liquid sloshing dynamics are validated with experimental results for a 1:10 scale LNG tank section. The simulation of external wave loading is validated with data from an experiment with wave run-up against a semi-submersible offshore structure. Both test cases show that modelling of two-phase effects can be beneficial for the simulation of hydrodynamic wave loading.

I. INTRODUCTION

Ships and offshore structures should be able to withstand environmental loads during violent weather conditions, even in case of steep, extreme, waves. Awareness of the magnitude of these loads is important during design and operation. In order to estimate wave loads on offshore structures by means of a numerical method, both the wave field and the structural geometry have to be modelled accurately. Linear wave theory only is rarely sufficient to describe wave dynamics during impact against a structure. The dynamics of the water and compressible air phases are well visible for complex free surface problems like green water loading, slamming and tank sloshing. In complex cases, modelling the dynamics of both water and the surrounding compressible air is helpful to estimate loads more accurately.

In particular around the free surface, a complex interaction between water and air may occur. Wave overtopping, either due to wave steepness or the presence of an offshore structure, may lead to the entrapment of large air pockets. They can have a cushioning effect on peak pressure levels during wave impacts [14]. The size of these air pockets varies greatly, but they generally have a short lifetime [3]. The entrapment of air pockets, and also of smaller entrained bubbles, is not only important for wave loading on ships and offshore structures (external wave loading), but also for internal wave loading cases, such as the fluid motion in fuel tanks or anti-roll tanks on board of a ship.

Model test campaigns to predict the air-water interaction during hydrodynamic wave loading are rather costly and time-consuming. Therefore, there is a great need for simulation tools that can predict the impact loadings on and the flow around offshore structures during hydrodynamic wave loading.

To model two-phase flow effects for wave-type problems, a number of choices have to be made with respect to the numerical method. The description of the fluid flow of both phases is based on the Navier–Stokes equations. These equations can be applied to both phases separately, but in the current method the liquid and gas phase are described as one aggregated fluid with varying properties. The grid should be constructed such that the free surface is described as 'sharp' as possible in order to model its dynamical behaviour sufficiently accurate.

An option would be to use a Lagrangian approach, but this becomes cumbersome for highly distorted and rapidly moving free surfaces, as is the case in many offshore problems. Also, SPH methods are not a competitive option as they are expensive and suffer from inaccurate pressure predictions. Thus we have opted for an Eulerian approach with a fixed Cartesian grid.

The description of the interface is based on the VOF method [7], with a local height function for improved accuracy [10], [20]. It is able to keep the interface sharp, while it allows use of a rather coarse grid to limit computation times. The numerical method, called COMFLOW, has been developed initially to simulate one-phase flow. Earlier applications were in the simulation of sloshing on board spacecraft [6], [20], [22], in medical science [11], [12] and in μ-gravity biology [13]. Currently, the method is used to solve engineering problems in the maritime and offshore industry [10], [21], [25]. Extensive

validation with model experiments that are relevant for the offshore industry is an important aspect in the development of the numerical method.

The basics of the numerical method are presented first in this paper, after which more attention is paid to the flow description around the free surface. The method is validated with the results of two series of model experiments: (i) the sloshing fluid motion inside a partially-filled LNG tank, and (ii) wave run-up against a semi-submersible offshore structure.

II. Mathematical model

A. Aggregated governing equations

The two-phase flow is described as the flow of one aggregated fluid with varying properties, described by one continuity and one momentum equation. This approach leads to a smooth velocity field around the free liquid surface [19].
– Mass conservation is applied on an arbitrary part Ω of the flow domain with boundary S and an outward directed normal vector $\mathbf{n}$:

$$\int_\Omega \frac{\partial \rho}{\partial t}\,\mathrm{d}\Omega + \oint_S \rho \mathbf{u}\cdot\mathbf{n}\,\mathrm{d}S = 0, \tag{1}$$

with $\mathbf{u} = (u, v, w)^T$ the velocity and ρ the density.
– Momentum conservation is expressed by

$$\int_\Omega \frac{\partial(\rho\mathbf{u})}{\partial t}\,\mathrm{d}\Omega + \oint_S (\rho\mathbf{u}\cdot\mathbf{n})\mathbf{u}\,\mathrm{d}S + \oint_S p\mathbf{n}\,\mathrm{d}S = \oint_S \{\mu(\nabla\mathbf{u} + \nabla\mathbf{u}^T) + \tfrac{2}{3}\mu(\nabla\cdot\mathbf{u})\mathbf{I}\}\cdot\mathbf{n}\,\mathrm{d}S + \int_\Omega \rho\mathbf{F}\,\mathrm{d}\Omega, \tag{2}$$

with pressure p, dynamic viscosity μ and external force $\mathbf{F}$.
– A polytropic equation of state

$$\frac{p}{p_{ref}} = \left(\frac{\rho}{\rho_{ref}}\right)^\gamma \text{ with } \gamma = 1.4 \tag{3}$$

is used to describe the compressibility of the flow. In this equation, the initial (atmospheric) reference values for pressure and density are used [25].

B. Boundary conditions

The no-slip boundary condition $(\mathbf{u} = 0)$ is used at solid walls and objects within the computational domain. Inflow and outflow boundary conditions are specified in case of open boundaries.

Incoming waves at the inflow boundary are specified by prescribing the incoming velocity. They are usually prescribed as a linear wave or a regular 5th-order Stokes wave [18], but can also be described as a user-defined superposition of cosines (design wave).

The outflow boundary requires special attention, as some of the wave components may not propagate through but reflect against the boundary. Conventional boundary conditions, such as the Von Neumann and Sommerfeld outflow boundary conditions, are available in the numerical method. The disturbing effect of wave reflections on the fluid distribution can be reduced by putting the boundaries further away from the flow region of interest. Another method that reduces the effect of reflections is the use of a numerical beach [9], however, this requires extension of the flow domain by at least one wavelength downstream of the structure.

To keep the computational domain as small as possible while minimizing reflections at boundaries, a Generating and Absorbing Boundary Condition (GABC) has been developed recently [4], [24]. This boundary condition implicitly computes an average phase velocity of the outgoing wave, and combines it with a Sommerfeld condition. This makes it possible to locate the outflow boundary close to the interesting flow area around a structure, which reduces the computational costs considerably.

III. Numerical discretisation

The computational domain is covered by a fixed Cartesian grid to solve the Navier–Stokes equation numerically. The variables are staggered, with velocities defined on cell faces, whereas pressure and density are defined in cell centers. As described in [10], the presence of solid body geometries is indicated by volume apertures and edge apertures. After identifying which grid cells are open for fluid flow, the 'open' cells are labelled as E(mpty), S(urface) and F(luid) cells. For two-phase flow calculations, the flow characteristics are resolved in all open cells. This prevents mass conservation problems (leading to local pressure spikes) that have been observed in one-phase simulations with rapid free surface advection [26]. After time discretization (and rearrangement of the density), the following set of equations is obtained

$$\frac{\rho^{n+1} - \rho^n}{\delta t} + \mathbf{u^n}\cdot\nabla\rho^{\mathbf{n}} + \rho^{\mathbf{n}}\nabla\cdot\mathbf{u^{n+1}} = \mathbf{0}, \tag{4}$$

$$\frac{\mathbf{u^{n+1}} - \mathbf{u^n}}{\delta t} + \frac{1}{\rho^n}\nabla p^{n+1} = \mathbf{R}^n, \tag{5}$$

where $\mathbf{R}$ contains the convective and diffusive terms, as well as the body forces. Diffusive terms are discretized in the usual way. Convection is treated in principle according to the symmetry-preserving approach of [23], however adding some artificial diffusion by first- or second-order upwinding. Especially in the second (air) phase the latter is a better choice in terms of kinetic energy dissipation [25]. Further, the pressure gradient is related to the divergence in the continuity equation [23].

A. Pressure calculation

Combining (4) and (5) leads to a Poisson-type equation from which the pressure can be computed. Actually, in the compressible area it is a hyperbolic wave equation, that has to be treated implicitly:

$$\delta t\nabla\cdot(\frac{1}{\rho^n}\nabla p^{n+1}) = \frac{1}{\rho^n}\left\{\frac{\rho^{n+1} - \rho^n}{\delta t} + \mathbf{u^n}\cdot\nabla\rho^{\mathbf{n}}\right\} + \nabla\cdot\mathbf{R}. \tag{6}$$

The term between braces in the right hand side stems from the continuity equation. As the density may vary up to a factor of 1000 in space or time around the free surface, the two embraced terms separately can become large, resulting in high

local flow velocities which could lead to innacuracies. But, note that this term represents the discrete Lagrangian derivative $D\rho/Dt$. As for incompressible flow this derivative is zero, we only have to take account of the gas density ρ_g. Denoting the open fraction of a cell by F_b, the liquid fraction in a cel by F_s (hence the gas fraction is $F_b - F_s$), and noting that DF_s/Dt =0, the expression between braces in (6) can be reduced to the discrete version of

$$\frac{D\rho}{Dt} = (F_b - F_s)\frac{D\rho_g}{Dt} = (F_b - F_s)\left(\frac{\partial \rho_g}{\partial t} + \mathbf{u}\cdot\nabla\rho_g\right). \quad (7)$$

This expression does never contain large contributions which have to cancel. Now, the equation of state (3) is used to express the gas density in (7) in terms of the pressure at the new time level: $\rho_g^{n+1} = \rho_g(p^{n+1})$. Before transferring this term to the left-hand side of the Poisson equation, it is linearized by a Newton approximation to eliminate the exponent $1/\gamma$ originating from the equation of state. After that, the Poisson matrix in (6) is solved by the BiCGSTAB method. For one-phase flow simulations, the pressure is solved using the SOR (Successive Over Relaxation) method, where the optimal relaxation parameter is determined during the iterations [2]. Application of the SOR method for two-phase simulations would lead to much longer calculation times due to the slow convergence behaviour of the method in case of large variations in density, leading to an unbalanced matrix.

IV. Towards a sharp free surface

Instead of smearing out, the free surface has to be kept sharp within one grid cell to be able to resolve violent flow conditions with breaking waves, droplets and bubbles accurately. Given the large density ratio around the interface, particular attention has to be paid to the density definition in cell centers and at cell edges.

A. Free surface description

As the free surface position is changing in time, the liquid filling ratios F_s and the free surface labels have to be recomputed every computational timestep. The free surface is described by the equation $F_s(\mathbf{x}, t) = 0$; its displacement is done in two steps: first the free surface is reconstructed and after that it is advected to the new position. The original VOF method [7] uses a Simple Linear Interface Calculation (SLIC), where the interface only consists of line segments that are constructed parallel or perpendicular to the major flow axes. With this approach there exist discontinuities of the free surface.

When using the piecewise linear reconstruction method (PLIC), introduced by Youngs [29], there are still free surface discontinuities at the cell edges and there is a jump in the free surface angle at each cell edge [6]. In three dimensions, the PLIC method represents the interface by oblique planes, and especially then the reconstruction of the free surface by the PLIC method leads to strongly enhanced computational costs.

B. Local height function

A characteristic drawback of the SLIC method is the unphysical creation of flotsam ('floating wreckage') and jetsam ('jettisoned goods'). These phenomena concern isolated, submesh-size droplets disconnected from the free surface because of errors induced by the free surface advection and subsequent reconstruction [15]. To prevent flotsam and jetsam, a local height function has been introduced [6]. For the original VOF method without height function, the VOF-values are rounded off at the end of the displacement algorithm (to keep the values between zero and one), leading to significant gains or losses in liquid mass, up to several percents of the initial water mass [9].

To determine the local height function, first the orientation of the free surface is determined (horizontal or vertical) depending on the values of the liquid filling ratio F_s in the surrounding block of cells. After that, the horizontal or vertical local height in each row or column in this block is determined by summing the VOF fractions (Fig. 1).

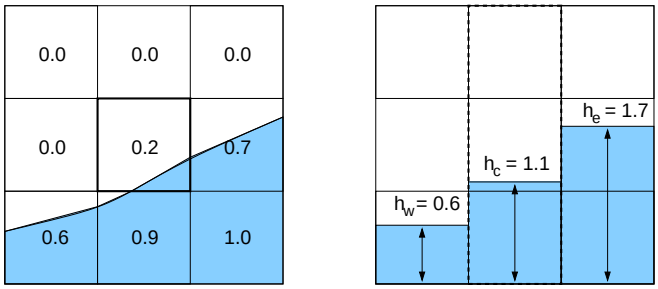

Fig. 1. Construction of the local height function in a 3x3 block for a central S-cell.

The local height function is applied in a 3×3 block in 2D, or a $3 \times 3 \times 3$ block in 3D, of cells surrounding a surface cell. Although other numerical methods take more grid cells (e.g. 3×5 or 3×7 in [1]) into account to determine the height function, using a $3 \times 3(\times 3)$ block is sufficient in the current numerical method. This is because the free surface is always captured in one grid cell: the central grid cell in Fig. 1 (where the orientation of the free surface is horizontal). When the free surface would cut the upper and lower edge of the central grid cell in Fig. 1, the height function is constructed vertically (by summing in horizontal direction) instead of horizontally. Upon using the local height function, flotsam and jetsam have almost disappeared. Also, the loss of water is much smaller than with the original VOF method [9].

C. Gravity-consistent discretisation

Discretisation of the density is not only important for the unsteady term in the continuity equation (1), but also for several terms in the momentum equation (2). Given the staggered arrangement of grid variables, pressure and density are both defined and computed in cell centers. For compressible two-phase flow, the density in the cell center is calculated as a cell

average

$$\rho = \frac{F_s}{F_b}\rho_l + \frac{(F_b - F_s)}{F_b}\rho_g, \tag{8}$$

Although the density is coupled to the pressure value in the cell centers, the staggered variable arrangement requires computation of densities at cell edges as well. This is the case in both the pressure gradient and the diffusion term. The calculation of the density at cell edges by averaging between cell center values seems to be straightforward. However, one main issue for the density averaging is the width of the averaging stencil.

Considering a vertical momentum equation in the cell edge at $(i, j+\frac{1}{2})$ (the central point in Fig. 2), an averaging method could take the complete grid cells (i, j) and $(i, j+1)$ into account (cell-weighted averaging), or only the top half of cell (i, j) and the bottom half of cell $(i, j+1)$ (control-volume weighted).

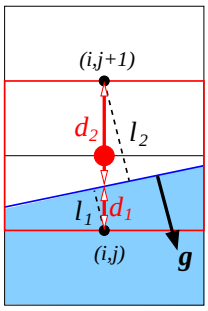

Fig. 2. *Normal distances l_1 and l_2 and intersection distances d_1 and d_2 used in the gravity-consistent density averaging method.*

Serious errors (spurious velocities) have been observed when applying cell-weighted averaging to compute the density at cell edges. It is argumented that these anomalies could be reduced by improving the estimation of the free surface curvature [16], improving flow algorithms [17] or by improving the surface tension description [5]. Francois et al. [5] address spurious velocities to the numerical imbalance of the surface tension and the associated pressure gradient. Their method reduces the spurious velocities for surface tension dominated cases. For offshore applications, however, the pressure gradient should also be in balance with the gravity force, as the gravity forcing is usually much larger than the surface tension force.

In particular, in equilibrium situations the hydrostatic pressure should be in balance with the gravity force, i.e. $\nabla p = \rho \boldsymbol{g}$. To ensure such a balance, a necessary condition is $\nabla \times (\rho \boldsymbol{g}) = 0$. For a constant density this is a trivial requirement, but not for a varying denisty. This leads to a requirement on the density averaging method discussed above.

One way to find the 'correct' way of averaging is to demand that it yields the exact hydrostatic pressure for equilibrium positions of the free surface. Thus consider the situation as in Fig. 2, with a gravity vector that may act under an angle with the z-coordinate; thus $\boldsymbol{g} = (g_x, -g_z)$. When we set the pressure at the free surface at 0, then the hydrostatic pressure in the point (i, j) is equal to $p_{i,j} = \rho_l |\boldsymbol{g}| l_1 = \rho_l g_z d_1$, whereas the 'aerostatic' pressure in the point $(i, j+1)$ is equal to $p_{i,j+1} = -\rho_g |\boldsymbol{g}| l_2 = -\rho_g g_z d_2$. Demanding that the pressure gradient at the cell face $(i, j+\frac{1}{2})$ discretely satisfies $\partial p/\partial z = -\rho g_z$ leads to the requirement

$$\frac{p_{i,j+1} - p_{i,j}}{\delta z} = -\rho_{i,j+\frac{1}{2}}\, g_z.$$

Substituting the above analytic values for p leads to the desired density averaging:

$$\rho_{i,j+\frac{1}{2}} = \frac{d_1\rho_l + d_2\rho_g}{d_1 + d_2}. \tag{9}$$

We note that this corresponds with averaging the density over the line (indicated in red in Fig. 2) connecting the cell centers; almost equivalently it is an average over the indicated momentum control volume. Because it complies with the (hydrostatic) gravitational part of the pressure gradient, we call this averaging 'gravity consistent'.

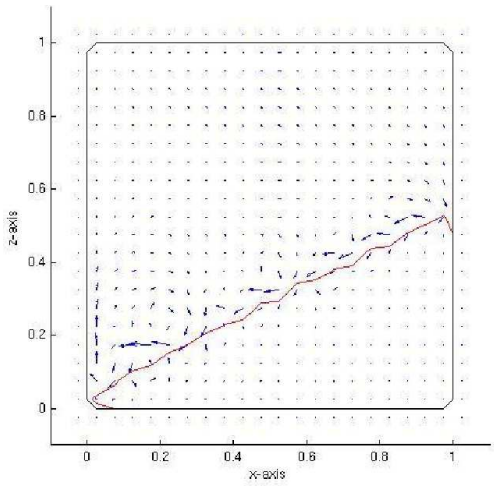

(a) Cell-weighted density averaging

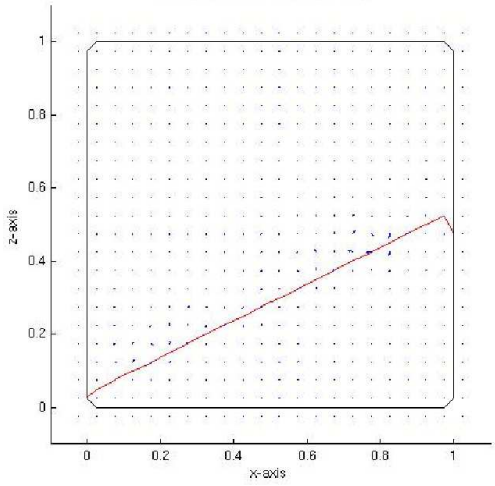

(b) Gravity-consistent density averaging

Fig. 3. *Spurious velocities due to cell-weighted averaging of density (top) disappear when a gravity-consistent density averaging is used (bottom).*

Fig. 3 shows velocity vectors from two calculations for an equilibrium surface as discussed in Fig. 2. The cell-weighted averaging clearly shows spurious velocities, whereas they disappear when gravity-consistent averaging is used.

Not only for this theoretical test case, but also for more realistic test cases, such as the sloshing motion of fluid inside a tank (Section V), the spurious velocities disappear and the description of the free surface improves (Fig. 4). The cell-weighted density averaging method leads to an unphysically irregular free surface, with many droplets in the air above the surface, (Fig. 4(a)). Furthermore, flow velocities in the enclosed air above the free surface are relatively high compared with the flow velocities in the liquid phase. When applying gravity-consistent averaging, the free surface is smoother (Fig. 4(b)) and agrees much better with experimentally observed fluid distributions.

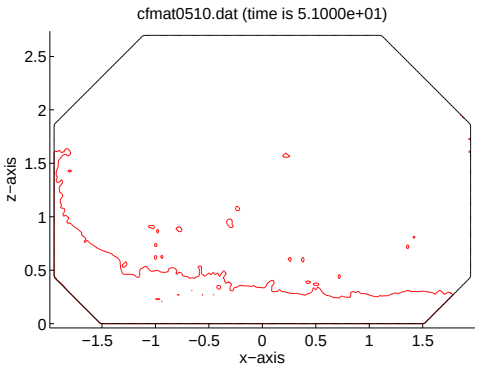

(a) Cell-weighted density averaging

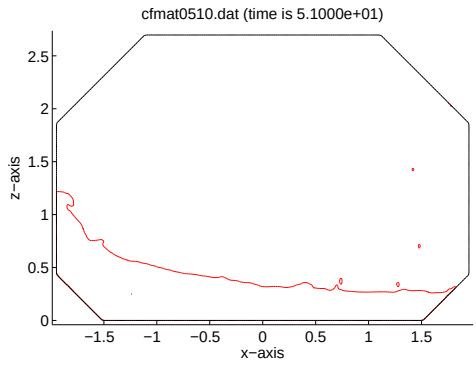

(b) Gravity-consistent density averaging

Fig. 4. *Effect of the density averaging method on the free surface for a regular sway sloshing experiment with* 10% *filling ratio.*

V. Validation for confined flow: sloshing

The sloshing fluid motion in partially-filled LNG tanks is an example of two-phase flow with complex interaction between both phases. The fluid motion in these tanks is investigated, both experimentally and numerically, to study impact loads on tank walls and its effect on ship motion [27], [28]. Model tests on scale 1:10 have been carried out to generate validation material ; the numerical simulations have been carried out on this same scale. The sloshing tank model is based on an LNG tank inside a No. 96 LNG carrier. The inner side of the tank has a width of $3897mm$ and a height of $2697mm$ on model scale. The tank is filled with water, while the front and back side are made of perspex to enable visualisation of the fluid motion inside the tank.

Irregular sway and roll tank motion

One of the test cases is an irregular sway and roll experiment with a filling ratio of 10%. The oscillation period is $10.6s$ on full scale, corresponding to $3.2s$ on model scale. The tank motion is irregular with wave breaking and air entrapment occuring occasionally.

During the first sloshing periods, the level of run-up against the tank wall varies considerably (Fig. 5). Simulation and

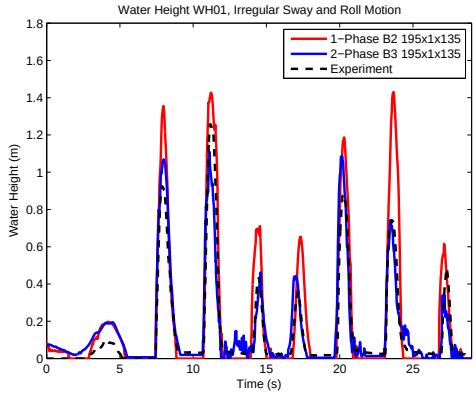

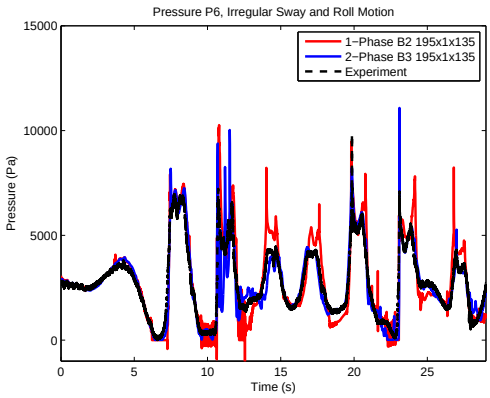

Fig. 5. *Water height development for* 10% *filling ratio irregular sway and roll test at the tank wall (WH01,* $x = 1.89m$*) and pressure signal at transducer P01 (*$x = 1.656m, z = 0.152m$*).*

experiment are in phase, but the one-phase simulation overestimates the run-up against the tank wall. This discrepancy might be related to the liquid motion that is not damped by the 'vacuum' in the remaining part of the flow domain. The second phase is more viscous in the two-phase simulation, leading to a better agreement between numerically predicted and experimentally observed water heights.

Fig. 5 shows the pressure development at transducer $P01$, located near the lower corner of the tank wall. When studying the pressure at the tank wall, similar conclusions as for the

water height can be drawn. The overestimated run-up motion in the one-phase simulation translates into peak pressures well above the experimentally observed values. Numerical pressure spikes are observed occasionally and are related to mass conservation problems in case of rapid transition from empty (void) cells to fluid cells. The pressure has to 'work' to achieve mass conservation for these cases, which manifests itself in spikes. The two-phase simulation gives a better pressure prediction, although some short-during pressure spikes are also observed here.

After start-up of the sloshing motion during the first few periods of the experiment, the irregularity of the sloshing motion results in an alternation of periods with an almost flat horizontal free surface and periods with violent flow conditions sometimes featuring air entrapment. One typical impact at $t = 140s$ is selected to be studied in more detail. Fig. 6

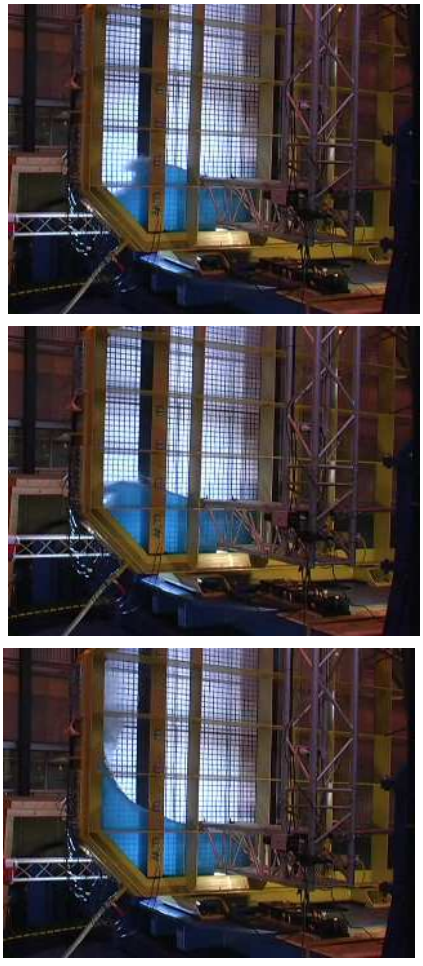

Fig. 6. *Video frames of irregular* 10% *irregular sway and roll test around* $t = 140s$*: just prior, during and after air entrapment at the tank wall.*

shows some video frames of the experiment before, during and just after air entrapment. The entrapped air pocket with a diameter of $O(10^{-1})m$ is only present during a short period of $O(10^{-1})s$, being compressed quickly by the water that is running up against the tank wall. The pressure development is considered for transducer $P01$, below the entrapped air pocket. Here the one-phase simulation shows a number of

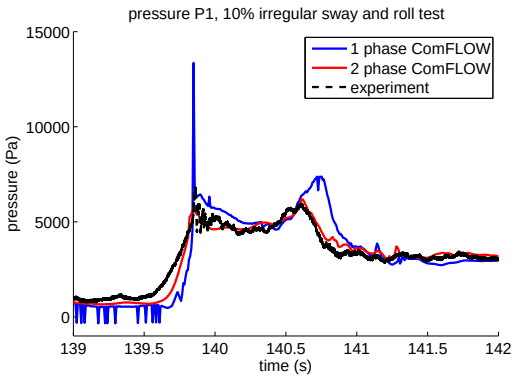

Fig. 7. *Pressure development for transducer* $P01$ *(*$x = 1.656m, z = 0.152m$*) during the air entrapment case shown in Fig. 6.*

pressure spikes that are present in neither the two-phase simulation nor the experiment (Fig. 7). Furthermore, there is a (small) time lag between the one-phase simulation and the experiment, while the two-phase simulation shows a pressure peak simultaneously with the pressure peak in the experiment.

VI. Validation for open flow domain: wave run-up

The effects of two-phase flow with respect to the propagation of waves in a domain with open boundaries are examined by investigating the wave run-up against a semi-submersible structure. Model experiments, scale $1 : 50$, have been carried out at MARIN to provide validation material for various aspects of the numerical method, such as the wave run-up effects and the impact loading on an offshore structure. The setup of the wave run-up model experiment is sketched in Fig. 8. A semi-submersible with a typical (but simplified) geometry is located in the center of the flow domain. On full scale, it has a length of $144.5m$, a width of $17.5m$, a height of $28.0m$ and a draft of $16.0m$. The waves in the experiment are

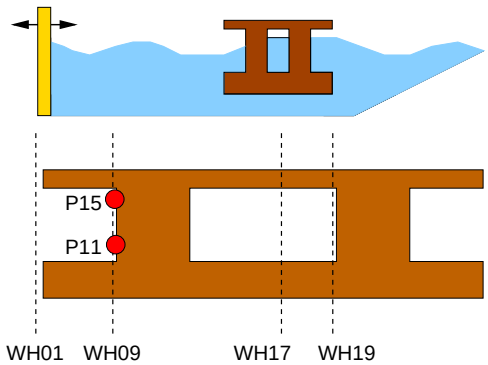

Fig. 8. *Schematisation of the wave run-up test setup (top) and position of selected wave probes and pressure transducers (bottom).*

generated by a flap-type wave generator. The basin width is $4m$, which is equal to $200m$ on full scale, with solid side walls. In the experiment, a beach is located downstream of the object

to damp the motion of outgoing waves and to prevent from wave reflections. To measure the wave elevation at several positions, an array of wave probes is placed in the basin. The pressure is monitored by 28 transducers that are fitted on the semi-submersible.

Wave run-up at the columns of the structure

To decrease the distance between the wave maker and the semi-submersible in the simulation, the incoming waves have been analyzed by wave calibration tests (without semi-submersible in the flow) to establish a representative incoming wave [8]. The generated incoming wave is modeled as a 5th order Stokes wave with wave parameters depending on the experiment. A Sommerfeld boundary condition is applied at the outflow boundary and the simulations are carried out for three wave periods.

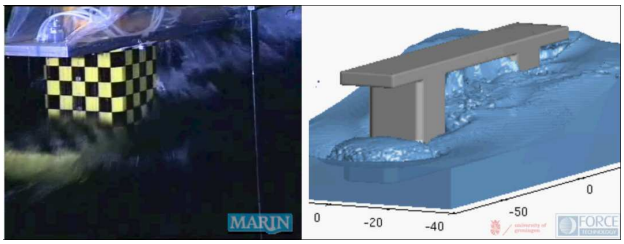

Fig. 9. Snapshots of experiment and simulation for the wave run-up case.

The incoming wave has a full scale wave height of $15.0m$ and a wave period of $11.0s$. To validate the simulations, the time interval between $t = 944s$ and $t = 970s$ of the experiment is selected, for which high-speed video frames are available. During wave impact, the first column is fully covered by liquid, while also the bottom of the extended deck is hit by the impacting wave. Fig. 10 shows the wave height development at the first column (probe WH09) and between the columns (probe WH17).

The simulations have been carried out on a grid of $154 \times 83 \times 55$ cells. The overall agreement between the wave heights in the simulations and the experiment is fairly good. The wave heights in Fig. 10 show a periodic variation between zero and maximum filling ratios at the columns of the semi-submersible. Between the two columns of the semi-submersible, the wave height in the two-phase simulation is closer to the experimental values for the wave peaks, while the agreement is worse (compared to the one-phase simulation) for the wave troughs.

The pressure development near the top ($P15$) and the bottom ($P11$) of the first column of the semi-submersible is shown in Fig. 11. For transducer $P11$, the short-lasting pressure peaks of the experiment are also visible in both simulations, but slightly lower. Near the top of the first column, at transducer $P15$, there are more pronounced differences between the one- and two-phase simulations and the experiment. The peak pressure values in the simulations are relatively low, which can be attributed to the limited number of grid

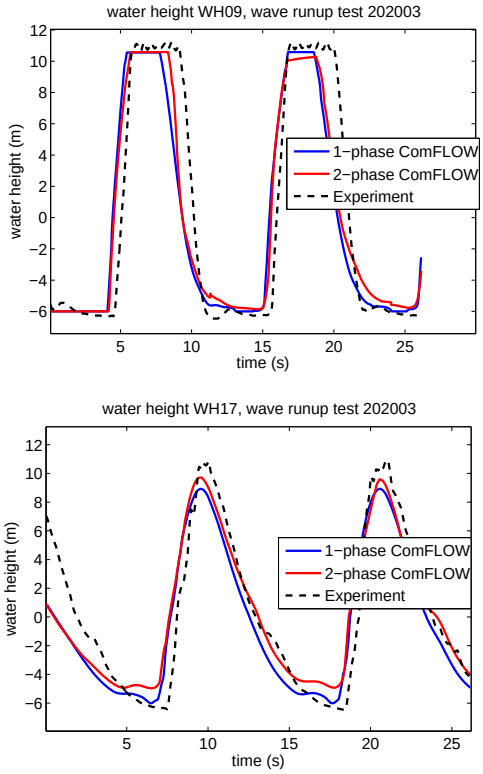

Fig. 10. *Wave height development for run-up at the first column (WH09, x = -39.76m), and wave height between the columns (WH17, x = 5.31m).*

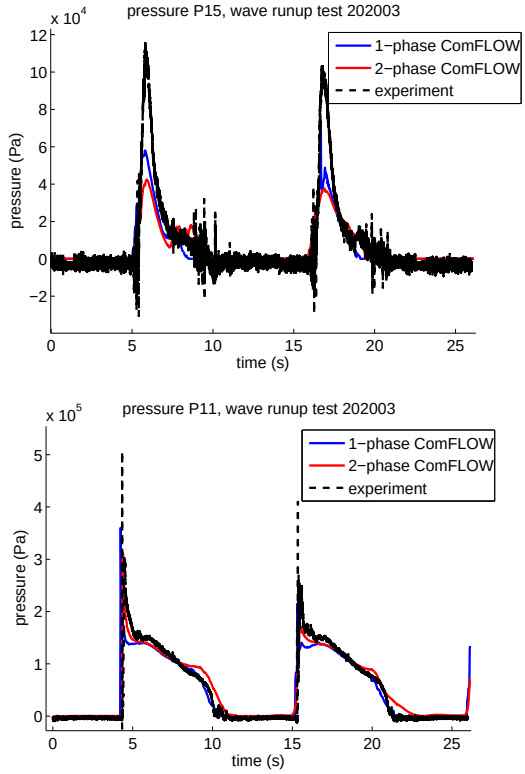

Fig. 11. *Pressure development at the first column ($x = -39.5m$): top (P15) and bottom of the column (P11).*

cells along the column. The difference in peak pressure values between one- and two-phase simulations can be attributed to the cushioning effect of the air between the wave front and the semi-submersible, reducing the peak pressure level. For one-phase flow, the water is not decelerated by the compressible air, leading to a slightly earlier and higher impact on the pressure transducers.

CONCLUDING REMARKS

Various offshore test cases have been simulated with the COMFLOW CFD code. In case of complex hydrodynamic phenomena such as wave breaking and air entrapment, it is beneficial to carry out two-phase flow simulations. The dynamics of the compressible second phase affects the fluid distribution and the pressure level of the liquid phase. Due to the presence of the second phase, the fluid density varies up to a factor of 1000 across the free surface, imposing a challenge to stability and convergence of the numerical method. Rewriting the pressure Poisson equation, application of an appropriate pressure solver and the use of a gravity-consistent density averaging method are essential ingredients of the numerical method to be able to handle these large density variations.

For confined flows, e.g. sloshing fluid in LNG tanks, highly unsteady flow phenomena such as air entrapment are resolved by the two-phase flow modeling in the numerical method. When simulating the flow in open domains, additional difficulties, such as wave definition and inflow and outflow boundary conditions, show up. Wave damping and reflection should be treated carefully for these cases. For the simulation of wave run-up against a semi-submersible offshore structure there is a good prediction of the flow around the structure, although a finer grid (e.g. through local grid refinement [21]) is needed to predict the impact on the columns and the deck of the structure accurately.

ACKNOWLEDGEMENTS

This research is supported by the Dutch Technology Foundation STW, applied science division of NWO and the technology programme of the Ministry of Economic Affairs in The Netherlands.

REFERENCES

[1] S. Afkhami and M. Bussmann. Height functions for applying contact angles to 2D VOF simulations. *Int. J. Num. Meth. Fluids*, 57(4):453–472, 2008.

[2] E.F.F. Botta and M.H.M. Ellenbroek. A modified SOR method for the Poisson equation in unsteady free-surface flow calculations. *J. Comput. Phys.*, 60:119–134, 1985.

[3] G.B. Deane and M.D. Stokes. Scale dependence of bubble creation mechanisms in breaking waves. *Nature*, 418:839–844, 2002.

[4] B. Duz, R.H.M. Huijsmans, P.R. Wellens, M.J.A. Borsboom, and A.E.P. Veldman. Towards a general-purpose open bounsdary condition for wave simulations. In *30th Conf. Ocean, Offshore Arctic Eng. OMAE2011*, paper OMAE2011-49979, Rotterdam, Netherlands, June 19-24, 2011.

[5] M.M. Francois, S.J. Cummins, E.D. Dendy, D.B. Kothe, J.M. Sicilian, and M.W. Williams. A balanced-force algorithm for continuous and sharp interfacial surface tension models within a volume tracking framework. *J. Comput. Phys.*, 213:141–173, 2006.

[6] J. Gerrits and A.E.P. Veldman. Dynamics of liquid-filled spacecraft. *J. Engng Math.*, 45:21–38, 2003.

[7] C.W. Hirt and B.D. Nichols. Volume of Fluid (VOF) method for the dynamics of free boundaries. *J. Comput. Phys.*, 39:201–225, 1981.

[8] B. Iwanowski, M. Lefranc, and R. Wemmenhove. Numerical simulation of sloshing in a tank, CFD calculations against model tests. In *28th Int. Conf. Offshore Mech. Arctic Engng*, paper OMAE2009-79051, Honolulu, Hawaii, USA, 2009.

[9] K.M.T. Kleefsman. *Water Impact Loading on Offshore Structures - A Numerical Study*. PhD thesis, University of Groningen, 2005.

[10] K.M.T. Kleefsman, G. Fekken, A.E.P. Veldman, B. Buchner, and B. Iwanowski. A volume-of-fluid based simulation method for wave impact problems. *J. Comput. Phys.*, 206:363–393, 2005.

[11] G.E. Loots, B. Hillen, and A.E.P. Veldman. The role of hemodynamics in the development of the outflow tract of the heart. *J. Engng Math.*, 45:91–104, 2003.

[12] N.M. Maurits, G.E. Loots, and A.E.P. Veldman. The influence of vessel wall elasticity and peripheral resistance on the flow wave form: CFD model compared to in-vivo ultrasound measurements. *J. Biomechanics*, 40(2):427–436, 2007.

[13] C. Nouri, R. Luppes, A.E.P. Veldman, J.A. Tuszynski, and R. Gordon. Rayleigh instability of the inverted one-cell amphibian embryo. *Physical Biology*, 5(1):article 010506, 2008.

[14] D.H. Peregrine. Water-wave impact on walls. *Ann. Rev. Fluid Mech.*, 35:23–43, 2003.

[15] W.J. Rider and D.B. Kothe. Reconstructing volume tracking. *J. Comput. Phys.*, 141:112–152, 1998.

[16] A. Rudman. A volume-tracking method for incompressible multifluid flows with large density variations. *Int. J. Num. Meth. Fluids*, 28:357–378, 1998.

[17] E. Shirani, N. Ashgriz, and J. Mostaghimi. Interface pressure calculation based on conservation of momentum for front capturing methods. *J. Comput. Phys.*, 203:154–175, 2005.

[18] L. Skjelbreia and J.A. Hendrickson. Fifth order gravity wave theory. In *Proc. 7th Coastal Engineering Conf.*, pages 184–196, The Hague, The Netherlands, 1960.

[19] G. Trygvasson, B. Bunner, A. Esmaeeli, D. Juric, N. Al-Rawahi, N. Tauber, J. Han, S. Nas, and Y.J. Jan. A front-tracking method for the computations of multiphase flow. *J. Comput. Phys.*, 169:708–759, 2001.

[20] A.E.P. Veldman, J. Gerrits, R. Luppes, J.A. Helder, and J.P.B. Vreeburg. The numerical simulation of liquid sloshing on board spacecraft. *J. Comput. Phys.*, 224:82–99, 2007.

[21] A.E.P. Veldman, R. Luppes, T. Bunnik, R.H.M. Huijsmans, B. Duz, B. Iwanowski, R. Wemmenhove, M.J.A. Borsboom, P.R. Wellens, H.J.L. van der Heiden, and P. van der Plas. Extreme wave impact on offshore platforms and coastal constructions. In *Proc. 30th Conf. Ocean, Offshore Arctic Eng. OMAE2011*, paper OMAE2011-49979, Rotterdam, Netherlands, June 19-24, 2011.

[22] A.E.P. Veldman and M.E.S. Vogels. Axisymmetric liquid sloshing under low gravity conditions. *Acta Astronautica*, 11:641–649, 1984.

[23] R.W.C.P. Verstappen and A.E.P. Veldman. Symmetry-preserving discretization of turbulent flow. *J. Comput. Phys.*, 187:343–368, 2007.

[24] P.R. Wellens. *Wave simulation in truncated domains for offshore applications*. PhD thesis, Delft University of Technology, 2012.

[25] R. Wemmenhove. *Numerical Simulation of Two-Phase Flow in Offshore Environments*. PhD thesis, University of Groningen, 2008.

[26] R. Wemmenhove, G.E. Loots, R. Luppes, and A.E.P. Veldman. Modelling two-phase flow with offshore applications. In *24th Int. Conf. Offshore Mech. Arctic Engng*, paper OMAE2005-67460, Halkidiki, Greece, 2005.

[27] R. Wemmenhove, R. Luppes, and A.E.P. Veldman. Application of a VOF method to model compressible two-phase flow in sloshing tanks. In *27th Int. Conf. Offshore Mech. Arctic Engng*, paper OMAE2008-57254, Estoril, Portugal, 2008.

[28] R. Wemmenhove, R. Luppes, A.E.P. Veldman, and T. Bunnik. Numerical simulation and model experiments of sloshing in LNG tanks. In *Computational Methods in Marine Engineering II*, Barcelona, Spain, 2007.

[29] D.L. Youngs. An interface tracking method for a 3d Eulerian hydrodynamics code. *Tech. Rep.* AWRE/44/92/35, Atomic Weapons Research Establishment, 1987.